

Polyp-Cavity Segmentation of Cold-Water Corals guided by Ambient Occlusion and Ambient Curvature

Kira Schmitt¹ and Jürgen Titschack^{2,3} and Daniel Baum¹

¹Zuse Institute Berlin (ZIB), Berlin, Germany

²MARUM - Center for Marine Environmental Sciences, University of Bremen, Bremen, Germany

³Senckenberg am Meer, Marine Research Department, Wilhelmshaven, Germany

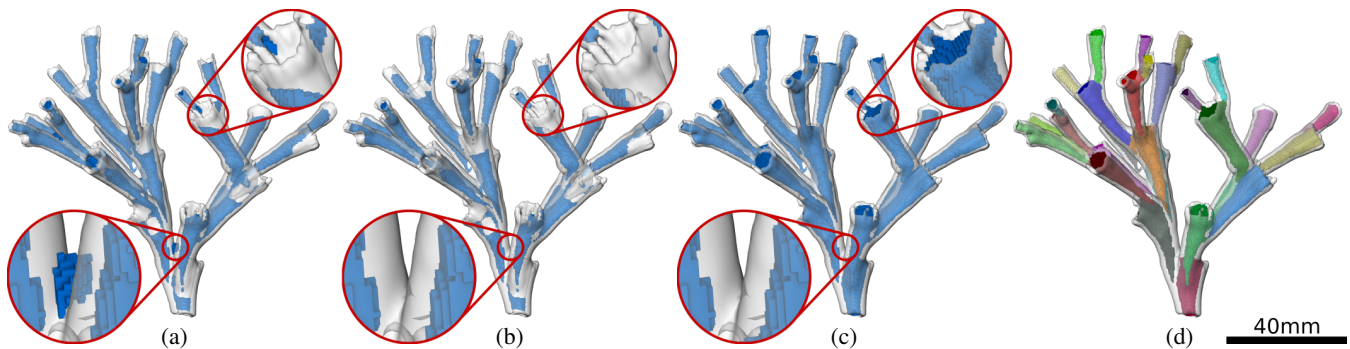


Figure 1: The proposed polyp-cavity segmentation method improves the results obtained with the ambient occlusion (AO) algorithm [BT16] by taking the curvature of the object into account. (a) The segmentation obtained by thresholding the AO field ($AO(x) \geq 0.7$). (b) An additional thresholding step based on the curvature ($AO(x) \geq 0.7$ and $AC(x) \geq 0.4$) excludes regions outside the polyp cavity, especially near joints. (c) Computing a minimal partition on a Gaussian mixture model trained on the AO, the ambient curvature, and the average distance fields gives a segmentation with filled polyp cavities and few to no false positives outside. (d) A contour-tree segmentation based on the random-walk distance transform [BWZ*19] gives the final instance segmentation of the polyp cavities.

Abstract

The segmentation of cavities in three-dimensional images of arbitrary objects is a difficult problem since the cavities are usually connected to the outside of the object without any difference in image intensity. Hence, the information whether a voxel belongs to a cavity or the outside needs to be derived from the ambient space. If a voxel is enclosed by object material, it is very likely that this voxel belongs to a cavity. However, there are dense structures where a voxel might still belong to the outside even though it is surrounded to a large degree by the object. This is, for example, the case for coral colonies. Therefore, additional information needs to be considered to distinguish between those cases. In this paper, we introduce the notion of ambient curvature, present an efficient way to compute it, and use it to segment coral polyp cavities by integrating it into the ambient occlusion framework. Moreover, we combine the ambient curvature with other ambient information in a Gaussian mixture model, trained from a few user scribbles, resulting in a significantly improved cavity segmentation. We showcase the superiority of our approach using four coral colonies of very different morphological types. While in this paper we restrict ourselves to coral data, we believe that the concept of ambient curvature is also useful for other data. Furthermore, our approach is not restricted to curvature but can be easily extended to exploit any properties given on an object's surface, thereby adjusting it to specific applications.

CCS Concepts

• Human-centered computing → Visual analytics; • Computing methodologies → Image processing; Image segmentation;

1. Introduction

Framework-forming scleractinian cold-water corals present important habitat engineers in the deep sea, where they build large reef structures along the upper continental slopes and outer continental shelves that form deep-sea biodiversity hotspots in water depths down to 1500 m [HR17; DG11]. Over time, these

reef structures might develop into large seafloor obstacles up to 380 m in height and several kilometers in lateral extent [MVD*06], called coral mound, which present important regional carbon(ate) sinks [TFB*16].

In contrast to shallow-water coral reefs that are formed by a high diversity of corals with various growth forms, only six cold-water

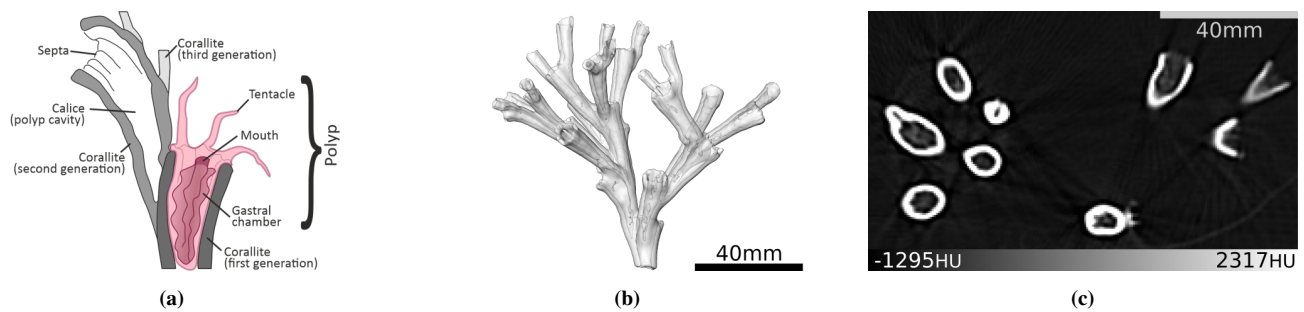


Figure 2: Cold-water corals. (a) The schematic depicts the typical parts of a cold-water coral. (b) The transparent iso-surface rendering shows the CT scan of C1W (100 HU). (c) The image shows a slice of the CT scan of C1W at $z = 130$ with the colormap ranging from the 5% quantile to the 95% quantile of the data.

corals are known to build reefs in the deep sea of which *Lophelia pertusa*, recently assigned to the genus *Desmophyllum* by Adamo et al. [AVS*16], represents the most important framework builder [WT17]. While the environmental preferences of *L. pertusa*, as well as the temporal development of coral mounds, is quite well studied [DG11; WT17], little is known about the impact of the high morphological plasticity of *L. pertusa* on the process of reef framework buildup and coral mound formation. Especially the lack of a quantitative and observer-independent methodology to investigate coral morphoplasticity, in respect to its corallite (individual skeletal units within coral colonies; [SF21]), colony and framework morphology, has hampered any further investigation so far. The first quantitative morphological assessment of *L. pertusa* by Sanna et al. [SF21] is based on time-consuming measurements by hand and was therefore limited to rather small fragments of coral colony (up to 33 corallites).

Computed tomography (CT) combined with advanced image processing allows to overcome this limitation and perform observer-independent quantitative morphological measurements, in principle independent of the colony-fragment size. Additionally, the three-dimensional CT scans allow the assessment of the spatial relationships between corallites and colony branches, thus providing also the opportunity to investigate the coral colony and framework morphology. However, any quantitative assessments of the morphoplasticity of corals must be based on a reliable segmentation (Fig. 1) of the corallites (part of the skeleton produced by one coral polyp; Fig. 2a) and the associated polyp cavity (calice: the cavity which the polyp lives in; Fig. 2a) within a specimen with high repetitious accuracy. Thereby, the polyp-cavity segmentation presents the first step.

The aim of this study is to improve its segmentation within specimens of *L. pertusa* compared to segmentations exclusively based on ambient occlusion [BT16], which typically contain also false segmentations on the outer surface of the coral skeleton, especially within dense, bushy coral colony morphotypes. To this end, we extend the previous work on ambient occlusion-based cavity segmentation [BT16] by introducing the concept of ambient curvature, defined as the curvature of the foreground seen from a point in the background, and including it into the segmentation procedure. This extension is based on the observation that cavities are mostly concave while the outside is mostly convex. The proposed

method was inspired by the work of Kronenberger et al. [KSHH18], who used voxel-based curvature estimation for the segmentation of fibers. Here, we show that by including the ambient curvature into the cavity segmentation process, we can significantly improve the segmentation of coral polyp cavities in two ways (Fig. 1). First, we reduce and, in fact, mostly completely eliminate false positives at the outside of cavities in comparison to only using ambient occlusion information. Second, while maintaining the first advantage, the cavities are filled to an even greater extent. The binary segmentation obtained with the proposed method is a prerequisite for further processing to obtain an instance segmentation of the polyp cavities (Fig. 1d), which again is the basis for any subsequent morphological analysis. In this paper, we make the following contributions:

- We introduce the concept of ambient curvature and present an efficient implementation for it.
- We present a novel approach to combine the information from ambient occlusion and ambient curvature using a Gaussian mixture model, followed by applying minimal partition, and show that we obtain superior results with this approach.
- We apply the approach to a set of coral specimens with diverse morphologies and show that we can successfully distinguish the coral polyp cavities from the outside even in very dense coral colony morphotypes, which we were not able to deal with before.

The remainder of the paper is structured as follows: In Section 2, we describe the coral data that we used in our study. Section 3 gives all the details of the methods being used. In Section 4, we present the results of applying our new approach to four distinctive coral data sets, followed by a discussion and an outlook in Section 5.

2. Data

For the comprehensive investigation of the morphoplasticity of *L. pertusa*, computed tomography (CT) scans of colony fragments from various cold-water coral reef sites distributed along the continental margins all over the North Atlantic will be investigated. The colony fragments were retrieved from the cold-water coral sites with dredges, giant box corers, and remotely operated vehicles (ROV) employed on various research vessels. For this study, four *L. pertusa* samples were selected with distinctive morphotypes:

- (I) sample C1W with slender corallites and an open, bushy colony morphotype (Fig. 2b);

- (II) sample *GeoB12738-1* with thick, compact corallites and a dense, bushy colony morphotype;
- (III) sample *TROND-CT10*, with slender corallites and a dense, bushy colony morphotype;
- (IV) and sample *SaM-ID43148* with slender corallites and a columnar colony morphotype.

The colony morphotypes have been qualitatively determined using the classification scheme of Sanna et al. [SF21].

Sample *CIW*, shown in Figure 2b,c, originates from Sula reef, off Norway, where it was taken with the submersible Jago during Poseidon cruise POS455 (position: 64.1110°N, 8.1187°E, 303 m water depth; white colourmorph; [FBH*14; BWF*19]). Sample *GeoB12738-1* (living colony; 34°59.98'N, 07°04.51'; 738 m water depth) was sampled during Pelagia cruise 64PE284 in the Meknes mud volcano area, Gulf of Cádiz with the MARUM ROV CHEROKEE [HWB*08]). Sample *TROND-CT10* was dredged by Wolfgang Berger in September 1980 in Trondheim fjord, Norway (63°36'N, 10°32'E, 50-90 m water depth). Sample *SaM-ID43148* was retrieved during Meteor cruise M70-1 with the ROV MARUM-Quest from the Gondola Slide, southeast of the Gargano Promontory in the Adriatic Sea (Station M70/1-752, GeoB11207, 41°43.51'N, 17°02.78'E, 710 m water depth). All selected specimens were scanned with a medical computed tomography device at Klinikum Bremen-Mitte, Gesundheit Nord, Bremen, Germany. Specimens *CIW* and *GeoB12738-1* were scanned with a Toshiba Aquilion 64 device (x-ray source voltage of 120 kV and a current of 600 mA, physical resolution: 0.35 mm in xy-direction and 0.5 mm resolution in z-direction, reconstruction interval in z-direction: 0.3 mm; reconstruction: Toshiba's patented helical cone beam reconstruction technique (TCOT)). Specimens *SaM-ID43148* and *TROND-CT10* were scanned with a Philips Brilliance iCT Elite 256 device (x-ray source voltage: 120 kV; current: 300 mA; physical resolution: 0.313 and 0.293 mm in xy-direction, respectively, 0.625 mm in z-direction; reconstruction interval in z-direction: 0.3 mm; reconstruction: filtered Back Projection (FBP) mode and a bone kernel (YB (Enhanced))).

3. Methods

As result of the CT scanning, for each of the samples, we obtain an intensity image $f: \mathcal{G} \mapsto \mathbb{R}$ defined on the voxel grid $\mathcal{G} = \{1, \dots, n_x\} \times \{1, \dots, n_y\} \times \{1, \dots, n_z\}$. From the intensity image, we derive a binary mask $\mathcal{B} \subset \mathcal{G}$ describing the objects surface. Intensity image and binary mask are the inputs to our method.

Some parts of the algorithm are easier understood in the continuous setting. In this case, we abuse the notation and denote the continuous version of the intensity image also by $f: \Omega \mapsto \mathbb{R}$ defined on the compact and convex set $\Omega \subset \mathbb{R}^3$, with $\mathcal{G} \subset \Omega$.

3.1. Overall workflow

The overall workflow is as follows: The binary mask \mathcal{B} is obtained from the intensity image f using simple thresholding. Then, the curvature is computed for f at each grid point of \mathcal{G} (Sect. 3.2). In the next step, the mask \mathcal{B} and the sign of the previously computed curvature are fed into the ambient occlusion algorithm

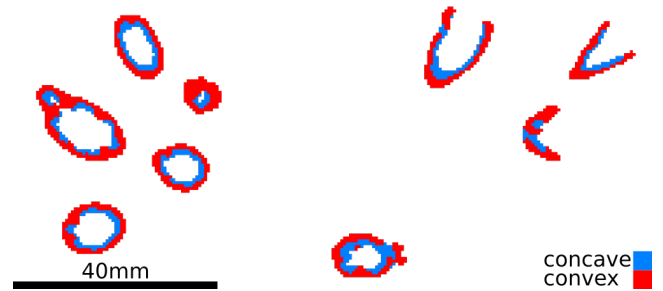


Figure 3: The surface of the coral is concave on the inside and convex on the outside. Here, the sign of the mean curvature is depicted for the voxels inside the binary coral mask \mathcal{B} (positive: convex; negative: concave).

(Sect. 3.3), resulting in three fields: the ambient occlusion, the average distance, and the ambient curvature field. From these fields and some trivial user scribbles, a Gaussian mixture model is computed (Sect. 3.4), the result of which is fed into a minimal partition algorithm (Sect. 3.5), computing an indicator field, which is thresholded in the final step to obtain the polyp-cavity segmentation. All intermediate results of the workflow, depicted in Figures 3-5, are illustrated on the cold-water coral *CIW* shown in Figure 2b.

3.2. Curvature estimation

The principal curvature values $\kappa_1, \kappa_2: \mathcal{G} \mapsto \mathbb{R}$ are computed with the method described by Rieger et al. [RTVV04] directly on the intensity image f . The sign of the mean curvature $H = \frac{1}{2}(\kappa_1 + \kappa_2)$ is positive for convex surface patches and negative for concave surface patches. We denote the sign field as

$$\xi(x) = \text{sign}(H(x)).$$

The method takes two parameters: The standard deviation $\sigma_{\text{curv, gradient}}$ of the Gaussian filter used to compute the derivatives of the image f , and the standard deviation $\sigma_{\text{curv, structure}}$ of the Gaussian filter in the structure tensor computation. The eigenvectors of the structure tensor are used to obtain a robust estimate for the normal vector of the local iso-surface at x with iso-value $f(x)$, as well as the principal directions. As recommended [RTVV04; WLB11], we keep both parameters as small as reasonable and fix them at $\sigma_{\text{curv, gradient}} = 1.0$ and $\sigma_{\text{curv, structure}} = 1.0$.

Finally, a small median filter with window size $3 \times 3 \times 3$ is applied to the sign field in order to reduce noise. The filtered sign field for *CIW* corresponding to the computational parameters given in Section 4.1 is shown in Figure 3.

3.3. Ambient occlusion

For the description of the ambient occlusion method, we follow our previous work [BT16] and the work by Correa and Ma [CM09] and define the ambient occlusion as

$$\text{AO}(x) = \frac{1}{4\pi} \int_{S^2} (1 - V_{\delta}(x, \omega)) d\omega,$$

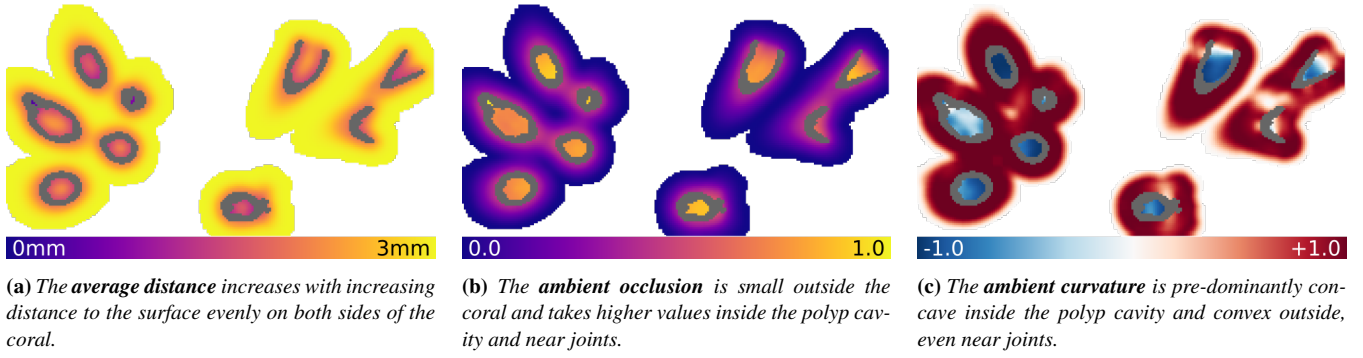


Figure 4: The ambient occlusion algorithm computes three features based on the coral’s surface represented by the binary coral mask (depicted in gray): The average distance (a), the ambient occlusion (b), and the ambient curvature (c). The features are only shown for voxels closer to the surface than the maximum ray length of 3 mm. The images show the same CT slice segment as in Figure 3.

with the visibility at voxel x along the direction $\omega \in S^2$ being defined as

$$V_\delta(x, \omega) = \begin{cases} 0 & , \text{ if } d_{\mathcal{B}}(x, \omega) < \delta \\ 1 & , \text{ otherwise} \end{cases}.$$

Here, $S^2 = \{\omega \in \mathbb{R}^3 : \|\omega\|_2 = 1\}$ denotes the three-dimensional unit-sphere. The parameter $\delta \in \mathbb{R}_{>0}$ is a user-defined distance threshold and $d_{\mathcal{B}}(x, \omega)$ is the distance from x to the closest point of \mathcal{B} :

$$d_{\mathcal{B}}(x, \omega) = \inf\{t \geq 0 : x + t\omega \in \mathcal{B}\}.$$

Additionally, the nearest surface point along the direction ω

$$\Pi_{\mathcal{B}}(x, \omega) = x + d_{\mathcal{B}}(x, \omega)\omega$$

is computed, if the distance is less than δ , and used to sample properties of the ambient surface around x . In particular, we use the curvature sign field ξ to define the **ambient curvature** as

$$AC(x) = \frac{1}{4\pi AO(x)} \int_{S^2} (1 - V_\delta(x, \omega)) \xi(\Pi_{\mathcal{B}}(x, \omega)) d\omega.$$

The ambient curvature is positive if the ambient surface is predominantly convex and negative if it is predominantly concave. The factor $\frac{1}{4\pi AO(x)}$ is a normalization factor since only rays hitting the surface are considered.

We also use the **average distance** field

$$AD(x) = \frac{1}{4\pi} \int_{S^2} \min\{d_{\mathcal{B}}(x, \omega), \delta\} d\omega,$$

which gives the average ray travel distance until the surface is hit.

In the discrete case, the ambient occlusion field is approximated with a finite set of $N \in \mathbb{N}_{>0}$ rays, so that

$$\overline{AO}_\delta(x) = \frac{1}{N} \sum_{i=1}^N (1 - V_\delta(x, \omega_i)).$$

The directions ω_i are drawn uniformly from the unit sphere S^2 . The ambient curvature and the average distance fields are computed similarly for the discrete case. The three ambient occlusion feature fields corresponding to the computational parameters given in Section 4.1 are shown in Figure 4.

3.4. Gaussian mixture model

Although a good segmentation of the polyp cavity can already be obtained by thresholding the ambient occlusion and ambient curvature fields, regions outside the cavities may still be falsely classified as being inside, as shown in Figure 1b. This happens especially near joints, where the ambient occlusion is high and the curvature indifferent due to the saddle point-like structure. In order to improve the segmentation, we build upon the ideas of the statistical and interactive segmentation framework described by Nieuwenhuis et al. [NTC11].

First, the user labels some regions inside and outside the polyp cavities with a few scribbles as shown in Figure 5a, resulting in two sets $\mathcal{B}_{\text{inside}} \subset \mathcal{G}$ and $\mathcal{B}_{\text{outside}} \subset \mathcal{G}$ containing the labeled voxels inside and outside the cavities, respectively.

Next, the ambient occlusion, ambient curvature, and average distance features are collected for all labeled voxels and used to fit a Gaussian mixture model. We write shortly

$$\mathcal{F}(x) = \begin{pmatrix} AO(x) \\ AC(x) \\ AD(x) \end{pmatrix} \in \mathbb{R}^3$$

for the ambient features of a voxel $x \in \mathcal{G}$.

The probability density function of a d -dimensional Gaussian mixture model with $M \in \mathbb{N}_{\geq 0}$ components, mixture weights $w_i \in \mathbb{R}_{\geq 0}$, means $\mu_i \in \mathbb{R}^d$ and covariance matrices $\Sigma_i \in \text{Sym}_+^d$ is defined as

$$p_{\text{GMM}}(y) = \sum_{i=1}^M w_i n(y|\mu_i, \Sigma_i)$$

where $y \in \mathbb{R}^d$ is the d -dimensional feature vector, $n(y|\mu_i, \Sigma_i)$ the d -dimensional multivariate normal distribution of the i -th component and the weights are normalized such that $\sum_{i=1}^M w_i = 1$. In our setting, $d = 3$ and y is the feature vector $\mathcal{F}(x)$. Although the number of components M can be left as a user adjustable parameter, we fix it to $M = 4$. The model parameters (w_i, μ_i, Σ_i) for $i = 1, \dots, M$ are fitted using the expectation-maximization algorithm [DLR77].

The mixture weights w_i are biased by the number of labeled vox-

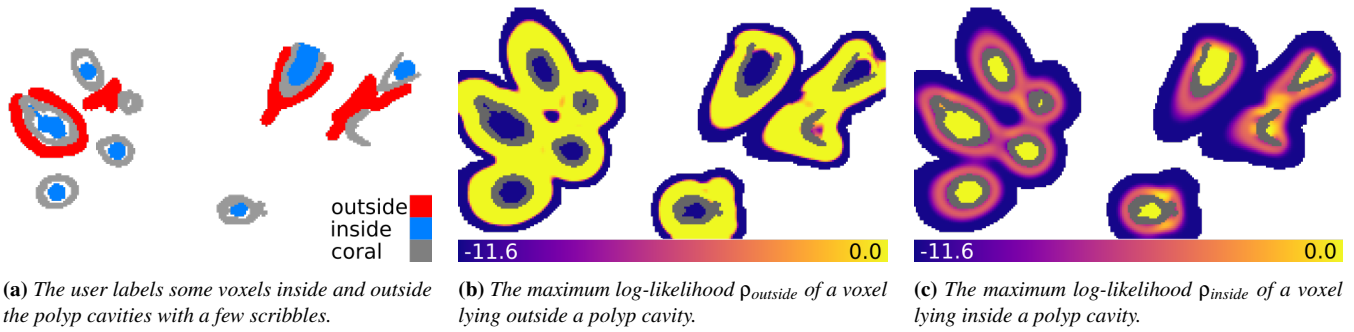


Figure 5: A Gaussian mixture model is fitted to the ambient occlusion features shown in Figure 4 and the user scribbles displayed in (a). The mixture is then evaluated for all voxels, yielding probabilities for being outside (b) and inside the polyp cavity (c). The images show the same CT slice segment as in Figure 3.

els in the component, e.g., when the user draws more scribbles in an area with similar features. Thus, we only use the log-likelihood of the maximum component to define the weight for a voxel being inside a polyp cavity as

$$\rho_{\text{inside}}(x) = \ln \left(\max_{i=1, \dots, M} n(\mathcal{F}(x) | \mu_{i, \text{inside}}, \Sigma_{i, \text{inside}}) + \varepsilon \right).$$

The weight ρ_{outside} for a voxel being outside is defined analogously. The numerical constant $\varepsilon = 10^{-6}$ is used to prevent the logarithm from going numerically unstable near 0 and effectively truncates the log-likelihood at $\ln(\varepsilon) \approx -11.51$. The weights for being outside a polyp cavity are shown in Figure 5b while the ones for being inside are shown in Figure 5c.

3.5. Minimal partition

Similar to the Nieuwenhuis et al. [NTC11] approach, a binary partition is computed based on the weights ρ_{inside} and ρ_{outside} by finding a set $I_{\text{inside}} \subset \Omega$ that minimizes the energy

$$\min_{I_{\text{inside}}} \int_{I_{\text{inside}}} -\rho_{\text{inside}} dx + \int_{\Omega \setminus I_{\text{inside}}} -\rho_{\text{outside}} dx + \int_{\partial I_{\text{inside}} \setminus \mathcal{B}} \lambda dS. \quad (1)$$

The first two terms favor a classification according to the voxel weights, while the last term penalizes a large surface area and suppresses small regions depending on the value of the regularization parameter $\lambda \in \mathbb{R}_{\geq 0}$. Notably, we only count the interface of the partitioning outside the coral skeleton $\partial I_{\text{inside}} \setminus \mathcal{B}$ instead of the whole interface $\partial I_{\text{inside}}$ in order to keep the interface between skeleton and cavity as is. The parameter $\lambda \in \mathbb{R}_{> 0}$ is user adjustable and depends on the expected surface area of the border between cavity (inside) and surrounding (outside).

An efficient convex approximation for Equation 1 was proposed by Pock et al. [PCCB09] and is based on a relaxation of the indicator variable for the set I_{inside} . The final model reads as

$$\min_{0 \leq u \leq 1} \int_{\Omega} (\rho_{\text{outside}} - \rho_{\text{inside}}) u + \int_{\Omega \setminus \mathcal{B}} \lambda \|\nabla u\|_2 dx, \quad (2)$$

with $u : \Omega \mapsto [0, 1]$ representing the indicator variable for I_{inside} . The minimization of Equation 2 is carried out iteratively with the

PDHGMp primal-dual algorithm [CP11]. The final binary segmentation is obtained by thresholding the continuous solution u :

$$I_{\text{inside}} = \left\{ x \in \Omega : u(x) \geq \frac{1}{2} \right\}.$$

4. Results

The presented results were computed on a desktop PC with the following configuration: CPU: Intel Core i9-10920X; GPU: Nvidia GeForce RTX 3090, 24 GiB VRAM; Memory: 128 GiB DDR4.

4.1. Computational parameters

All four cold-water coral samples described in Section 2 were processed with the same parameters. A threshold of 100 HU was used for computing the binary mask \mathcal{B} from the intensity images, exemplarily shown in Figure 2b.

The scale space parameter used to compute the Gaussian derivatives in the curvature estimation was set to $\sigma_{\text{curv, gradient}} = 1.0$ as previously recommended [RTVV04; WLB11], the standard deviation of the Gaussian filter in the structure tensor to $\sigma_{\text{curv, structure}} = 1.0$, and the median filter window to $3 \times 3 \times 3$ voxels.

The ambient occlusion was approximated with $N = 100$ rays and a mean filter with a window size of $5 \times 5 \times 5$ voxels was applied to smooth the results and to reduce the number of rays, as described in the previous work [TBM*18]. The maximum ray length was set to $\delta = 3$ mm, which is roughly the mean radius of the polyp cavities.

The user scribbles were drawn for each sample anew. The respective slices were chosen such that they contain joints and polyps in close proximity, as well as full cavities. This made sure that all features occurring inside and outside the polyp cavities were present in the training data for the mixture model. For the coral samples used in this paper, it was sufficient to draw scribbles on at most four slices. For CIW, all scribbles are visible in Figure 5a.

The number of components for both Gaussian mixture models was set to $M = 4$.

For the minimal partition method, the regularization parameter was set to $\lambda = 32.0$ and 1000 PDHGMp iterations were carried out.

Sample No.	Sample	Size	Curvature Estimation	Ambient Occlusion	Gaussian Mixture Model	Minimal Partition	Overall
(I)	C1W	$275 \times 145 \times 276$	5 s	14 s	1 s	1 s	21 s
(II)	GeoB12738-1	$512 \times 512 \times 375$	41 s	2 min 1 s	6 s	10 s	2 min 57 s
(III)	TROND-CT10	$799 \times 672 \times 622$	2 min 17 s	6 min 51 s	16 s	34 s	9 min 59 s
(IV)	SaM-ID43148	$1024 \times 729 \times 1215$	6 min 1 s	19 min 47 s	41 s	1 min 32 s	28 min 1 s

Table 1: Runtimes for each step of the segmentation workflow.

4.2. Cavity segmentation

In this section, we present qualitative results of the three different methods that were compared. Recall that we are interested in segmentations that fill the cavities as much as possible without including false positives outside the cavities, e.g., in branching regions. The results are shown in Figures 1,6-8. The quality of the cavity filling can be assessed by visually comparing the segmentations as well as by looking at the right insets of Figure 1. All other insets in Figures 1,6-8 highlight false positives, that is, regions segmented outside the cavities. Further false positives can be identified by zooming in to the electronic version of the manuscript.

In Figures 1,6-8, subfigure (a) always shows the segmentation obtained solely by thresholding the ambient occlusion field with $AO(x) \geq 0.7$. A smaller threshold would lead to more false positives outside the polyp cavities, especially near the joints and regions inside the colony. A larger threshold, on the other hand, would result in the polyp cavities being filled to a smaller degree. The segmentation approach purely based on ambient occlusion completely fails for the bushy, dense colonies shown in Figures 6,7, that is, it produces many false positives while filling many cavities only halfway, see subfigures (a).

Incorporating ambient curvature into the segmentation (Figs. 1,6-8, subfigures (b)) by thresholding additionally with $AC \geq 0.4$ already excludes regions outside the polyp cavities. Most notably, the segmentation results inside the bushy colonies improve substantially (Figs. 6b, 7b).

The final segmentation obtained by computing the minimal partition on the Gaussian mixture model gives near perfect results (Figs. 1,6-8, subfigures (c)). Only very few or no voxels outside the polyp cavities are labeled incorrectly and the cavities are filled very well. The segmentation also succeeds in the bio-eroded parts of the *GeoB12747-1* sample, as can be seen in Figure 9.

4.3. Performance

Table 1 lists the runtimes for each sample. Most time in our prototypical implementation, which was done in the software framework of Amira [SWH05], was spent on the estimation of the curvature and on computing the ambient occlusion features. The overall processing time, however, is still less than 30 min even for large datasets with approximately 1000^3 voxels. In addition to this, some manual labor is needed to draw the user scribbles. However, for each of the four datasets presented here, only a few minutes were needed to perform this task.

5. Discussion & Outlook

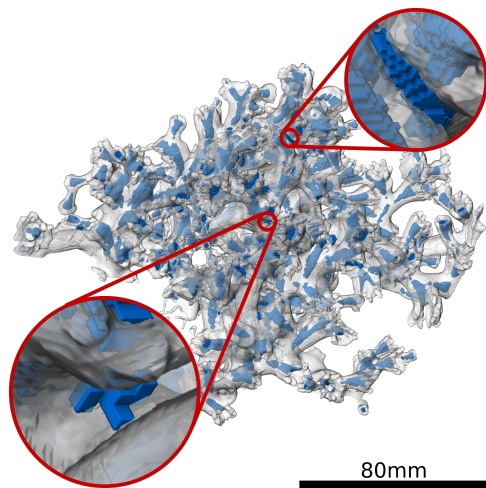
The presented approach works remarkably well for a wide range of coral morphotypes (Figs. 1,6-8). The used parameters were identified empirically, but it turned out that the choice of parameters did not depend on the coral's morphotype and runs, with the exception of the scribble step, fully automatic. For the actual cavity segmentation, only the ray length parameter δ in the ambient occlusion computation and the regularization parameter λ for the interface penalty in the binary segmentation are of major interest. In the project that motivated this work, a few hundred of such datasets will finally have to be processed. Since we carefully selected specimens with very different morphotypes, we are optimistic that the used parameters will also work for the other coral specimens. However, drawing scribbles for a few hundred datasets is still a lot of work despite the fact that it takes only a few minutes per dataset. Therefore, in future work, we will explore the use of a pre-trained Gaussian mixture model for different coral types as to eliminate this interaction step as well.

This work is part of a larger project in which hundreds of coral samples will be analyzed. This is only feasible if the overall runtime for a segmentation is small. Most of the algorithms used in the presented work have been implemented on the GPU with the exception of the curvature estimation and the smoothing of the ambient feature fields. This lead to feasible runtimes even for large volumes, however, we expect and hope to achieve further improvements on the runtime once these steps have also been optimized.

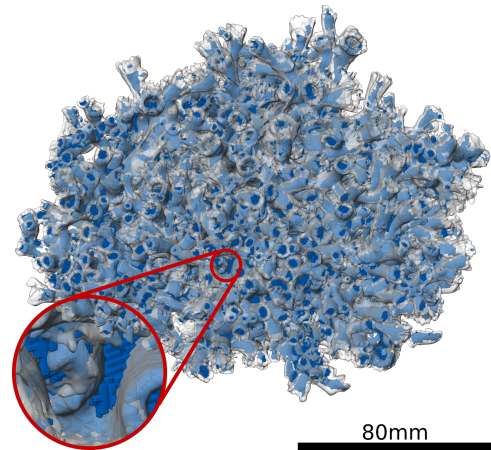
One major advantage of the method is that it is not a blackbox approach. The influence of all parameters on the results can be interpreted and explored interactively. Especially the two most influential parameters, the ray length truncation value δ in the ambient occlusion computation and the regularization parameter λ in the minimal partition computation. A good rule of thumb for the ray length is the mean radius of the cavities that should be segmented, so that the rays inside the cavity are just long enough to touch the surface. Since the minimal partition computation is fast, the actual value of the regularization parameter can be explored interactively, should it be necessary to be adjusted.

In future work, we will also explore the use of a scale space approach and train a Gaussian mixture model with the ambient occlusion fields obtained by multiple ray lengths. We expect that this approach will be able to further improve the segmentation results.

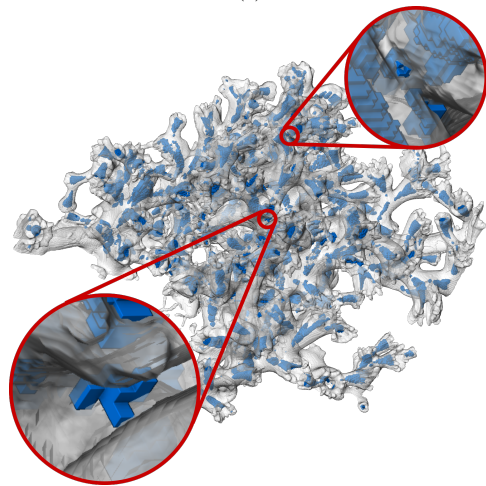
The focus of this study was the reduction of false positives outside the polyp cavities. However, after thorough visual inspection including an expert, we could also find very few to no false negatives, i.e. polyp cavities that are not detected or filled. In subsequent



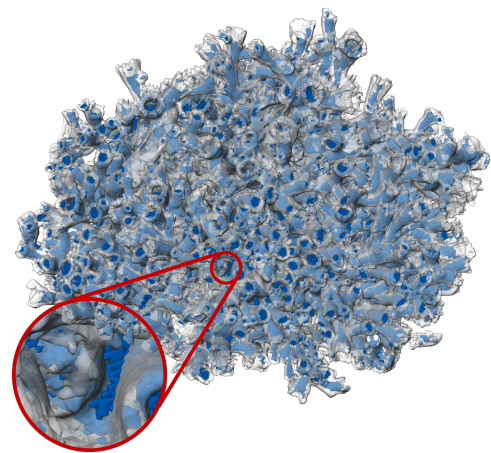
(a) $AO(x) \geq 0.7$



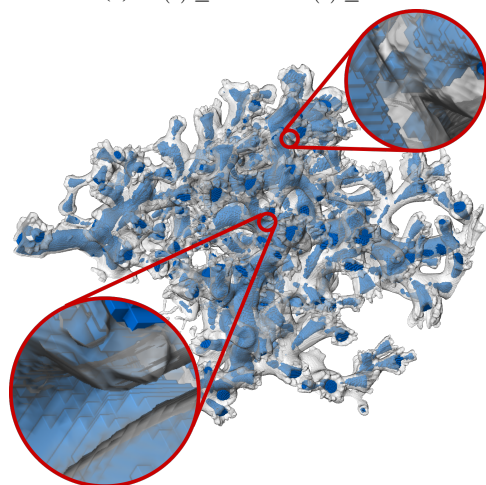
(a) $AO(x) \geq 0.7$



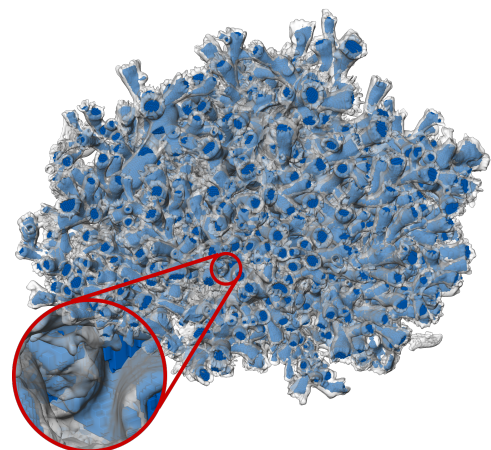
(b) $AO(x) \geq 0.7$ and $AC(x) \geq 0.4$



(b) $AO(x) \geq 0.7$ and $AC(x) \geq 0.4$



(c) minimal partition



(c) minimal partition

Figure 6: Segmentation results for the GeoB12738-1 sample.

Figure 7: Segmentation results for the TROND-CT10 sample.

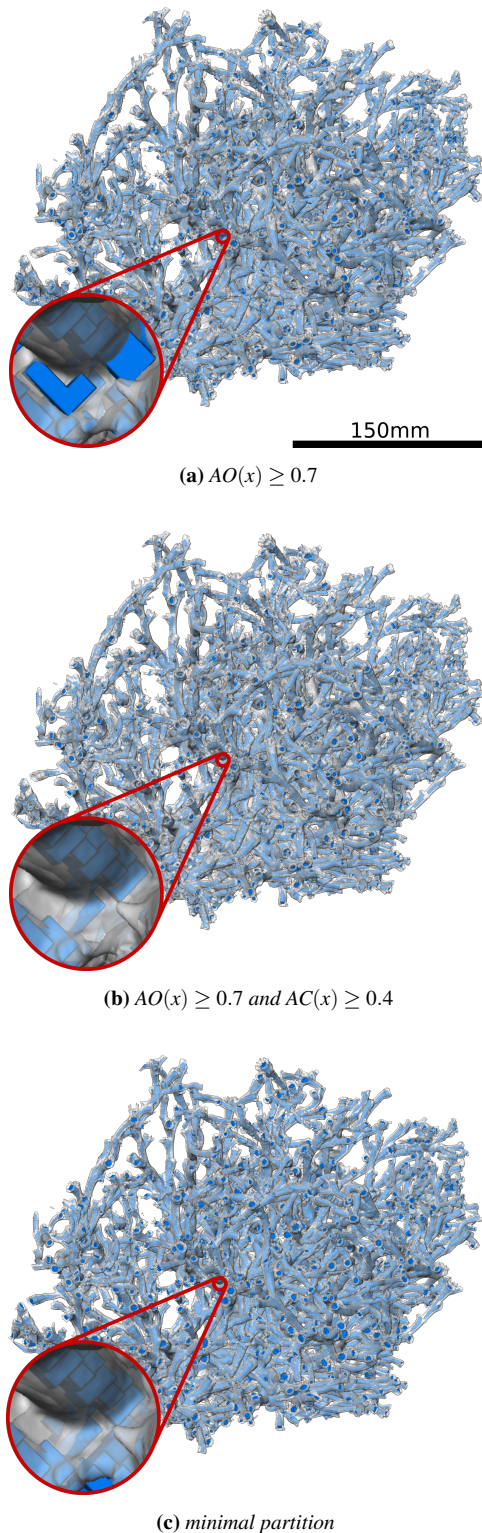


Figure 8: Segmentation results for the SaM-ID43148 sample.

work, we plan to evaluate the overall performance also quantitatively using annotated data when they become available.

In future studies, we will also examine the performance of our method on bio-eroded coral skeletons. Bioerosion in cold-water corals is mainly caused by boring sponges [FW98]. Their boring traces are visible as small molds in the coral skeletons [BVS*07] and alter the skeleton shape considerably which biases any subsequent shape analysis of the coral morphotypes. Consequently, its detection, segmentation and removal presents an important future task in the project. First results on the *GeoB12747-1* sample are promising (Fig. 9).

Another obstacle in the segmentation of the whole coral colony are long tube-like cavities that occur commonly in coral colonies and are caused by the polychaete *Eunice norvegica*, which lives in symbiosis with the corals [MLMvO13]. This polychaete produces parchment-like tubes within the living coral framework that gets subsequently calcified by the coral. Again, the proposed approach also deals well with these structures (Fig. 10).

Our cavity segmentation approach was motivated by a project on cold-water corals. For the analysis of these specimens, it turned out that the novel concept of ambient curvature was key to improving the cavity segmentation. Since curvature plays an important role in the characterization of many objects, we anticipate that ambient curvature will also help in the segmentation of quite different objects. For example, we had similar problems as with polyp-cavity segmentation when segmenting the cavities of crab claws [EFB*20]; we could not fill them to the extent that we would have liked without also segmenting regions outside the cavities. The use of ambient curvature could also directly improve the segmentation of bryozoan cavities [MTBF15]. However, we would like to point out that not only curvature but all properties that can be computed on the surface of an object can also be used in the framework of ambient occlusion computation. This might have a large potential for future work.

Data availability

The four original CT scans used in this paper as well as the final segmentation results have been submitted to the PANGAEA data repository.

- *CIW*
<https://doi.pangaea.de/10.1594/PANGAEA.947276>
- *GeoB12738-1*
<https://doi.pangaea.de/10.1594/PANGAEA.947334>
- *TROND-CT10*
<https://doi.pangaea.de/10.1594/PANGAEA.947308>
- *SaM-ID43148*
<https://doi.pangaea.de/10.1594/PANGAEA.947300>

Acknowledgment

We thank Markus Kronenberger (Fraunhofer ITWM, Kaiserslautern) for guidance with the curvature estimation. Arne-Jörn

Lemke and Christian Timann, Klinikum Bremen-Mitte, Gesundheit Nord (Bremen), are acknowledged for performing the CT scans and their support during the measurements. We thank Armin Form (GEOMAR), Gerold Wefer, Claudia Wienberg (both MARUM), André Freiwald and Giovanni Sanna (both Senckenberg am Meer) for providing the *Lophelia pertusa* CT scan of CIW (BMBF project BIOACID II (FKZ 03F0655A)) and for providing access to the TROND-CT10 sample taken by Wolfgang Berger, GeoB12738-1 and SaM-ID43148, respectively. Furthermore, we thank the nautical and scientific crews and especially the chief scientists of RV POSEIDON cruise POS455, PV PELAGIA cruise 64PE284, and RV METEOR cruise M70-1 during which the samples were retrieved. The work in this paper is part of the project “CTcoral – CyberTaxonomic Classification and Morphological Characterisation of Cold-Water Corals” funded by the Deutsche Forschungsgemeinschaft (DFG, German Research Foundation; Ba5042/6-1; Ti706/6-1) as project 490665120.

References

- [AVS*16] ADDAMO, ANNA MARIA, VERTINO, AGOSTINA, STOLARSKI, JAROSLAW, et al. “TI - Merging scleractinian genera: the overwhelming genetic similarity between solitary Desmophyllum and colonial Lophelia”. *BMC Evolutionary Biology* 16 (May 2016), 1471–2148. DOI: [10.1186/s12862-016-0654-8](https://doi.org/10.1186/s12862-016-0654-8) 2.
- [BT16] BAUM, DANIEL and TITSCHACK, JÜRGEN. “Cavity and Pore Segmentation in 3D Images with Ambient Occlusion”. *EuroVis 2016 - Short Papers*. Ed. by BERTINI, ENRICO, ELMQVIST, NIKLAS, and WISCHGOLL, THOMAS. The Eurographics Association, 2016. ISBN: 978-3-03868-014-7. DOI: [10.2312/eurovisshort.20161171](https://doi.org/10.2312/eurovisshort.20161171) 1–3.
- [BVS*07] BEUCK, LYDIA, VERTINO, AGOSTINA, STEPINA, ELIZAVETA, et al. “Skeletal response of *Lophelia pertusa* (Scleractinia) to bioeroding sponge infestation visualised with micro-computed tomography”. *Facies* 53 (2007), 157–176. ISSN: 0172-9179. DOI: [10.1007/s10347-006-0094-9](https://doi.org/10.1007/s10347-006-0094-9) 8.
- [BWF*19] BÜSCHER, J., WISSHAK, M., FORM, A., et al. “In situ growth and bioerosion rates of *Lophelia pertusa* in a Norwegian fjord and open shelf cold-water coral habitat”. *PeerJ* 7:e7586 (2019) 3.
- [BWZ*19] BAUM, DANIEL, WEAVER, JAMES C, ZLOTNIKOV, IGOR, et al. “High-throughput segmentation of tiled biological structures using random-walk distance transforms”. *Integrative and Comparative Biology* 59.6 (2019), 1700–1712 1.
- [CM09] CORREA, CARLOS and MA, KWAN-LIU. “The Occlusion Spectrum for Volume Classification and Visualization”. *IEEE Transactions on Visualization and Computer Graphics* 15.6 (2009), 1465–1472. DOI: [10.1109/TVCG.2009.189](https://doi.org/10.1109/TVCG.2009.189) 3.
- [CP11] CHAMBOLLE, ANTONIN and POCK, THOMAS. “A First-Order Primal-Dual Algorithm for Convex Problems with Applications to Imaging”. *Journal of Mathematical Imaging and Vision* 40 (2011), 120–125. DOI: [10.1007/s10851-010-0251-1](https://doi.org/10.1007/s10851-010-0251-1) 5.
- [DG11] DAVIES, ANDREW J. and GUINOTTE, JOHN M. “Global Habitat Suitability for Framework-Forming Cold-Water Corals”. *PLOS ONE* 6.4 (Apr. 2011), 1–15. DOI: [10.1371/journal.pone.0018483](https://doi.org/10.1371/journal.pone.0018483) 1, 2.
- [DLR77] DEMPSTER, A. P., LAIRD, N. M., and RUBIN, D. B. “Maximum Likelihood from Incomplete Data via the EM Algorithm”. *Journal of the Royal Statistical Society. Series B (Methodological)* 39.1 (1977), 1–38. ISSN: 00359246. URL: <http://www.jstor.org/stable/2984875> (visited on 06/03/2022) 4.
- [EFB*20] EGE, YANNIC C, FOTH, CHRISTIAN, BAUM, DANIEL, et al. “Adapting spherical-harmonics-based geometric morphometrics (SPHARM) for 3D images containing large cavity openings using ambient occlusion: a study with hermit crab claw shape variability”. *Zoomorphology* 139.3 (2020), 421–432 8.
- [FBH*14] FORM, A. U., BÜSCHER, J., HISSMANN, K., et al. unpublished report, 2014, 29. URL: https://www.geomar.de/fileadmin/content/zentrum/ze/fs/Poseidon_Berichte_2013_PDF/POS455_Form.pdf 3.
- [FW98] FREIWALD, ANDRÉ and WILSON, JOHN B. “Taphonomy of modern deep, cold-temperate water coral reefs”. *Historical Biology* 13.1 (1998), 37–52. DOI: [10.1080/08912969809386571](https://doi.org/10.1080/08912969809386571) 8.
- [HR17] HENRY, LEA-ANNE and ROBERTS, J. MURRAY. “Global Biodiversity in Cold-Water Coral Reef Ecosystems”. *Marine Animal Forests: The Ecology of Benthic Biodiversity Hotspots*. Ed. by ROSSI, SERGIO, BRAMANTI, LORENZO, GORI, ANDREA, and OREJAS, COVADONGA. Cham: Springer International Publishing, 2017, 235–256. ISBN: 978-3-319-21012-4. DOI: [10.1007/978-3-319-21012-4_6](https://doi.org/10.1007/978-3-319-21012-4_6) 1.
- [HWB*08] HEBBELN, DIERK, WIENBERG, CLAUDIA, BEUCK, LYDIA, et al. Vol. 265. 2008, 90. URL: [urn:nbn:de:gbv:46-ep001037383](https://nbn-resolving.org/urn:nbn:de:gbv:46-ep001037383).
- [KSHH18] KRONENBERGER, MARKUS, SCHLADITZ, KATJA, HAMANN, BERND, and HAGEN, HANS. “Fiber segmentation in crack regions of steel fiber reinforced concrete using principal curvature”. *Image Analysis & Stereology* 37.2 (2018), 127–137 2.
- [MLMvO13] MUELLER, CHRISTINA E., LUNDÄLV, TOMAS, MIDDELBURG, JACK J., and van OEVELEN, DICK. “The symbiosis between *Lophelia pertusa* and *Eunice norvegica* stimulates coral calcification and worm assimilation”. *PLOS ONE* 8 (2013), e58660. DOI: [10.1371/journal.pone.0058660](https://doi.org/10.1371/journal.pone.0058660) 8.
- [MTBF15] MATSUYAMA, KEI, TITSCHACK, JÜRGEN, BAUM, DANIEL, and FREIWALD, ANDRÉ. “Two new species of erect Bryozoa (Gymnolaemata) and the application of non-destructive imaging methods for quantitative taxonomy”. *Zootaxa* 4020.1 (2015), 81–100 8.
- [MVD*06] MIENIS, F, VAN WEERING, T, DE HAAS, H, et al. “Carbonate mound development at the SW Rockall Trough margin based on high resolution TOBI and seismic recording”. *Marine Geology* 233 (2006), 1–19. DOI: [10.1016/j.margeo.2006.08.003](https://doi.org/10.1016/j.margeo.2006.08.003) 1.
- [NTC11] NIEUWENHUIS, CLAUDIA, TÖPPE, ENO, and CREMERS, DANIEL. “Space-Varying Color Distributions for Interactive Multiregion Segmentation: Discrete versus Continuous Approaches”. *Energy Minimization Methods in Computer Vision and Pattern Recognition*. Ed. by BOYKOV, YURI, KAHL, FREDRIK, LEMPITSKY, VICTOR, and SCHMIDT, FRANK R. Berlin, Heidelberg: Springer Berlin Heidelberg, 2011, 177–190. ISBN: 978-3-642-23094-3 4, 5.
- [PCCB09] POCK, THOMAS, CHAMBOLLE, ANTONIN, CREMERS, DANIEL, and BISCHOF, HORST. “A convex relaxation approach for computing minimal partitions”. *2009 IEEE Conference on Computer Vision and Pattern Recognition*. 2009, 810–817. DOI: [10.1109/CVPR.2009.5206604](https://doi.org/10.1109/CVPR.2009.5206604) 5.
- [RTVV04] RIEGER, BERND, TIMMERMANS, FREDERIK, VAN VLIET, LUCAS, and VERBEEK, PIET. “On curvature estimation of ISO surfaces in 3D gray-value images and the computation of shape descriptors”. *IEEE transactions on pattern analysis and machine intelligence* 26 (Sept. 2004), 1088–94. DOI: [10.1109/TPAMI.2004.50](https://doi.org/10.1109/TPAMI.2004.50) 3, 5.
- [SF21] SANNA, GIOVANNI and FREIWALD, ANDRÉ. “Deciphering the composite morphological diversity of *Lophelia pertusa*, a cosmopolitan deep-water ecosystem engineer”. *Ecosphere* 12.11 (2021), e03802. DOI: <https://doi.org/10.1002/ecs2.3802> 2, 3.
- [SWH05] STALLING, DETLEV, WESTERHOFF, MALTE, and HEGE, HANS-CHRISTIAN. “Amira: a Highly Interactive System for Visual Data Analysis”. *The Visualization Handbook*. Elsevier, 2005, 749–767 6.
- [TBM*18] TITSCHACK, JÜRGEN, BAUM, DANIEL, MATSUYAMA, KEI, et al. “Ambient occlusion—A powerful algorithm to segment shell and skeletal intrapores in computed tomography data”. *Computers & Geosciences* 115 (2018), 75–87 5.
- [TFB*16] TITSCHACK, JÜRGEN, FINK, HISKE G., BAUM, DANIEL, et al. “Mediterranean cold-water corals – an important regional carbonate factory?”. *The Depositional Record* 2.1 (2016), 74–96. DOI: [10.1002/dep2.14](https://doi.org/10.1002/dep2.14) 1.

[WLB11] WERNERSSON, ERIK, LUENGO HENDRIKS, CRIS, and BRUN, ANDERS. "Accurate Estimation of Gaussian and Mean Curvature in Volumetric Images". May 2011, 312–317. DOI: [10.1109/3DIMPVT.2011.463.5](https://doi.org/10.1109/3DIMPVT.2011.463.5).

[WT17] WIENBERG, CLAUDIA and TITSCHACK, JÜRGEN. "Framework-Forming Scleractinian Cold-Water Corals Through Space and Time: A Late Quaternary North Atlantic Perspective". *Marine Animal Forests: The Ecology of Benthic Biodiversity Hotspots*. Ed. by ROSSI, SERGIO, BRAMANTI, LORENZO, GORI, ANDREA, and OREJAS SAGO DEL VALLE, COVADONGA. Cham: Springer International Publishing, 2017, 699–732. DOI: [10.1007/978-3-319-17001-5_16-12](https://doi.org/10.1007/978-3-319-17001-5_16-12).

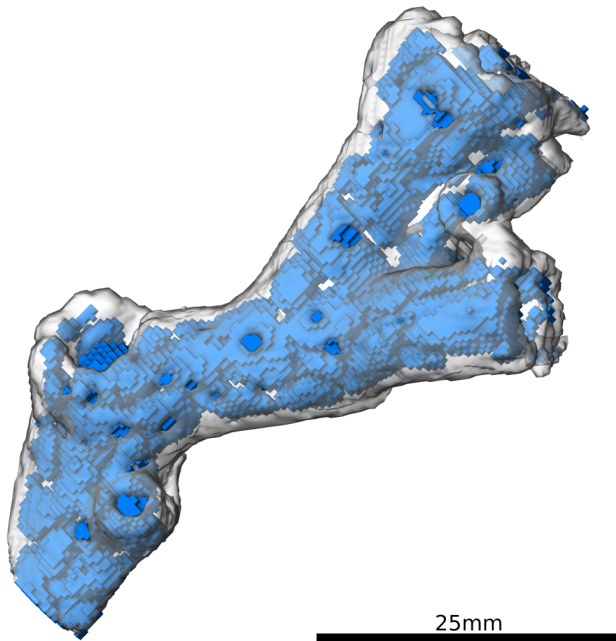
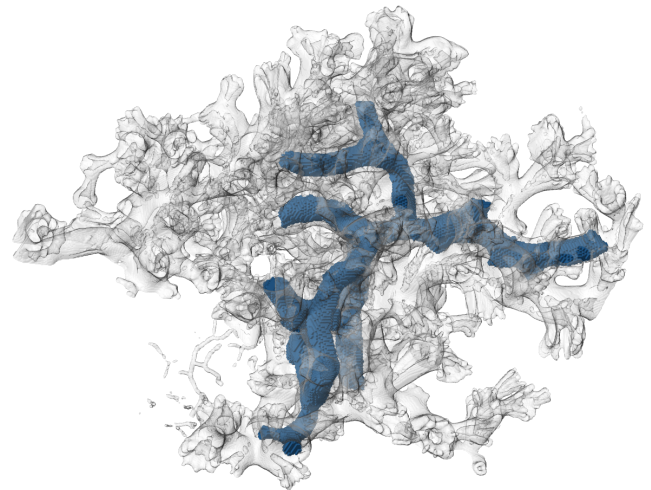
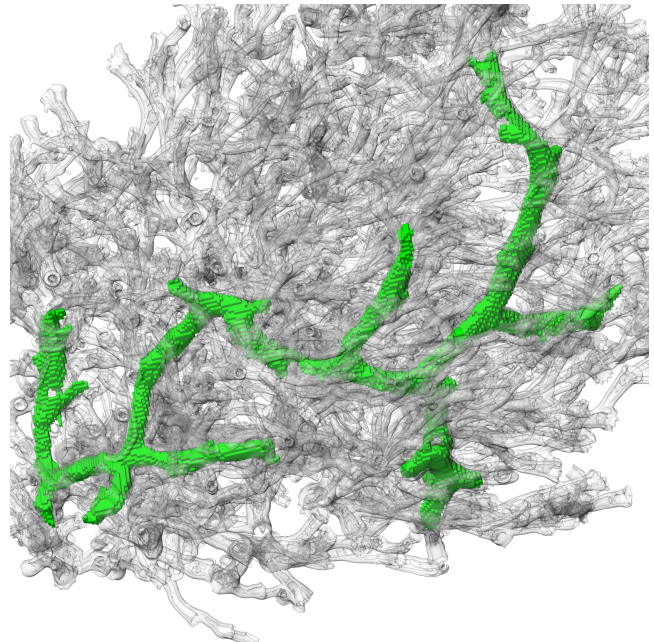


Figure 9: The segmentation is even robust in bio-eroded regions, shown here for a part of the sample GeoB12738 taken on the Pelagia cruise 64PE284.



(a) A *Eunice norvegica* tube in the GeoB12738 sample.



(b) A *Eunice norvegica* tube in the SaM-ID43148 sample.

Figure 10: The segmentation approach also succeeds in detecting the tubes of the polychaete *Eunice norvegica* within the coral skeleton.